INL/JOU-22-67217-Revision-0

Magnetostrictive Ultrasonic Waveguide Transducer for In-Pile Thermometry

July 2022

Drew Keller, Braden Robinson, Alex Draper, Amanda White, Zhangxian Deng, Joshua E Daw

Changing the World's Energy Future

Idaho National Laboratory

INL is a U.S. Department of Energy National Laboratory operated by Battelle Energy Alliance, LLC

INL/JOU-22-67217-Revision-0

Magnetostrictive Ultrasonic Waveguide Transducer for In-Pile Thermometry

Drew Keller, Braden Robinson, Alex Draper, Amanda White, Zhangxian Deng, Joshua E Daw

July 2022

Idaho National Laboratory
Idaho Falls, Idaho 83415

http://www.inl.gov

Prepared for the
U.S. Department of Energy
Under DOE Idaho Operations Office
Contract DE-AC07-05ID14517

Magnetostrictive Ultrasonic Waveguide Transducer for In-Pile Thermometry

Drew Keller, Braden Robinson, Alex Draper, Amanda White, Joshua Daw, Zhangxian Deng, *Member, IEEE*

Real-time, reliable temperature measurement for nuclear fuels is crucial for the safe operation of existing pressurized-water reactors and future advanced nuclear reactors. Magnetostrictive materials deform when subjected to a magnetic field, or exhibit magnetization variation when stressed. Based on these unique properties, this study prototyped an ultrasonic thermometer (UT) consisting of a magnetostrictive waveguide, a DC coil for providing appropriate magnetic biasing, and an AC coil for generating an acoustic impulse and detecting the resulting acoustic echoes. By tracking the time-of-flight between the pulse excitation and the echoes, the UT can detect nuclear fuel cladding temperature from a long distance. In this study, magnetostrictive iron-gallium alloys (i.e., Galfenol) were selected to configure the UT, due to their large magnetostriction, superior temperature survivability, excellent radiation resilience, and high mechanical robustness. A multiphysics finite element model considering electrical, magnetic, and mechanical dynamics in the magnetostrictive UT was then developed. The modeling error for time-of-flight was under 0.24%. Such accuracy enabled computer-aided design and guided the signal processing in this study. Eventually, the Galfenol-based UT was characterized at up to 120°C and benchmarked against an existing magnetostrictive UT based on iron-cobalt-vanadium alloys (i.e., Remendur). The sensitivities of Galfenol- and Remendur-based UTs are 162.8 10^{-6}/°C and 107.3$\times10^{-6}$/°C, respectively. Both waveguides exhibited superior linearity within the selected temperature range.

***Index Terms*—Galfenol, ultrasonic transducers, magnetostrictive, multiphysics modeling, thermometry**

I. Introduction

A total of 11 core melt accidents have occurred worldwide since 1952, including the famous Chernobyl and Fukushima disasters [1]. Therefore, reliable and real-time measurement of nuclear fuel rod temperatures is paramount to reactor safety, as the number of worldwide operational nuclear reactors increased from 230 to 443 from 2009 to 2019 [2], [3]. Ideally, in-pile thermometers must fit in tight spaces inside fuel claddings, withstand gamma and neutron flux radiation, and detect centerline temperatures exceeding 1500°C [3]. Current techniques include melt wire sensors, thermocouples, and linear variable differential transformer (LVDT) expansion thermometers [3]. Melt wire sensors are a large collection of metals whose melting points spread out at intervals of 5–12°C. They can only record a maximum temperature, not a temperature profile [3]. Type-K and type-N thermocouples can provide continuous temperature profiles at up to 1260°C, but exhibit significant thermal drift and limited lifespans [4]. Tungsten-rhenium thermocouples have demonstrated survivability at up to 2100°C while experiencing transmutation decalibration [5]. LVDT affords indirect temperature measurement by tracking the thermal expansion of a rod connected to the LVDT core [6]. Because the LVDT must be positioned close to the point of measurement, its measurement range is constrained by coil oxidation, coil insulation degradation, and the Curie temperature of the LVDT core [7].

Metals soften and their speed of sound reduces as the ambient temperature increases. Based on this working principle, previous studies have devised ultrasonic thermometers (UTs) consisting of metal waveguides and ultrasonic transducers for in-pile temperature monitoring [8], [9]. By using a long waveguide, ultrasonic transducers can be positioned away from extreme temperatures or corrosive environments [5]. Carlson *et al.* systematically explored refractory metals (e.g., stainless steel and titanium) as waveguide materials, and confirmed their feasibility for ultrasonic thermometry at up to 2900°C [10]. But the existing piezoelectric ultrasonic transducers used in UTs either exhibit relatively low mechanical robustness or degrade rapidly in high-temperature and irradiation environments [8].

The Joule effect describes a property of magnetostrictive materials that causes them to deform when subjected to a magnetic field [11], [12]. Magnetostrictive materials also exhibit magnetization variation, or the Villari effect, when stressed [13], [11], [14]. These unique properties have resulted in innovative ultrasonic transducer designs [13], [15], [16]. By welding magnetostrictive iron-cobalt-vanadium (Remendur) ultrasonic transducers to the refractory metal waveguides, Daw *et al.* devised and verified a Remendur-based magnetostrictive UT at up to 800°C [17]. However, Remendur is not ideal for radioactive environments, since cobalt atoms in Remendur will be irradiated due to neutron activation. Magnetostrictive iron-gallium alloys (Galfenol), on the other hand, are of particular interest to nuclear applications, because of their steel-like mechanical robustness [18], high Curie temperature ($\sim$700°C) [19], [20], [11], large field-induced strain ($\sim400\times10^{-6}$) [21], [22], and superior radiation tolerance ($>8.68\times10^{20}\mathrm{n/cm^2}$ neutron fluence and $>7.23\times10^{21}\gamma/\mathrm{cm^2}$ gamma fluence) [8]. Currently, no theoretical models are available to guide the development of Galfenol-based UTs. Experimental validation of Galfenol-based UTs is also lacking.

This study first prototyped a Galfenol-based UT operating

This work was supported in part through the Department of Energy (DOE) Advanced Sensors and Instrumentation program under DOE Idaho Operations Office Contract DE-AC07-05ID14517. The views and opinions of authors expressed herein do not necessarily state or reflect those of the U.S. Government or any agency thereof.

Drew Keller, Braden Robinson, Alex Draper, Amanda White, and Zhangxian Deng are with the Department of Mechanical and Biomedical Engineering, Boise State University, Boise, ID 83725 USA (e-mail: zhangxiandeng@boisestate.edu).

Joshua Daw is with the High Temperature Test Laboratory, Idaho National Laboratory, Idaho Falls, ID 83415 USA.

Manuscript received November xx, 2021.

in pulse-echo mode. An equivalent circuit model was then derived to identify system resonance. A multiphysics finite element model that accounted for the electrical, mechanical, and magnetic dynamics in Galfenol-based UTs was later developed. This model was used to optimize the UT signal-to-noise ratio and guide signal post-processing. Finally, the Galfenol-based UT was experimentally validated at up to 120°C and benchmarked against a Remendur-based UT.

II. Ultrasonic Thermometer Design

A. Thermometer Configuration

Figure 1 shows the new magnetostrictive UT developed in this study. The Galfenol waveguide is 0.83 mm in radius and 111.29 mm in length, which is cut from a <100>-oriented, highly textured, polycrystalline, and unannealed Galfenol rod (at 18.6 wt.% Ga) using electrical discharge machining. A 120-turn DC coil (40 turns per layer) made from 18 AWG (American Wire Gauge) polyester-coated copper wires is wrapped around a 3-D-printed polylactide bobbin and driven by a B&K precision DC power supply for the purpose of offering appropriate magnetic field biasing along the Galfenol waveguide. Unlike the permanent magnet biasing used in previous magnetostrictive UTs, the DC coil is more tolerant to harsh environments if high-temperature wires (e.g., ceramic-coated Inconel) and refractory bobbins (e.g., alumina) are used. Previous studies also confirmed that the magnetic biasing offered by a DC coil fosters more significant magnetostrictive responses than those offered by permanent magnets [23]. A 100-turn AC coil (50 turns per layer) made from 32 AWG polyester-coated copper wires is secured right in the center of the DC coil bobbin through press fitting. Driven by a pulse-echo transducer (EUT3160 from US Ultratek), the AC coil induces a longitudinal magnetic field pulse, thus initiating an impulsive acoustic wave in the Galfenol waveguide. The echoes from the ends of the Galfenol waveguide later generate voltage signals across the AC coil in return. The voltage signal is filtered by a 12 kHz-9 MHz bandpass filter, and ambient temperature data can be derived from the time-of-flight between the impulse excitation and the resulting reflections.

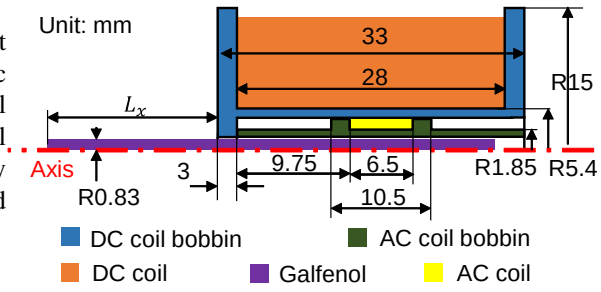

(a)

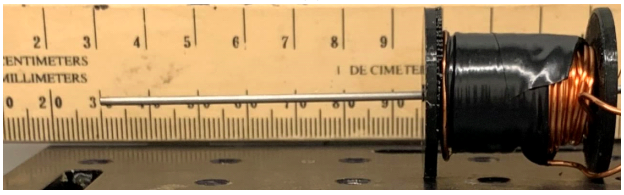

(b)

Fig. 1: (a) 2-D axisymmetric cross-sectional view and (b) physical assembly of Galfenol-based UT.

B. Design Parameters

Preliminary experiments showed magnetostrictive UT performance to be sensitive to the following parameters:

- **Electrical excitation.** The Ultratek pulse-echo transducer can output a tone burst signal with customized fundamental frequency f_0 and magnitude V_0. The signal-to-noise ratio available from the UT first improves as V_0 increases. Further increasing V_0 distorts the UT waveforms and introduces nonlinearity in time-of-flight measurement, due to the magnetic-field-induced Young's modulus variation in Galfenol or the Delta-E effect [24], [25]. Therefore, to maintain the "small perturbation" assumption and alleviate the Delta-E effect, the tone burst setting in the Ultratek system is set to $V_0 = 100$ V, resulting in a $\sim$0.6 V magnitude tone burst across the AC coil. To maximize the energy coupling efficiency between the AC coil and the Galfenol waveguide, the tone burst frequency f_0 is selected to match one of the waveguide's natural frequencies.
- **Current through the DC coil.** The current through the DC coil is noted as I_0. The Galfenol waveguide exhibits the most significant magneto-mechanical coupling when it operates at its "burst region," where the magnetic energy offered by the DC coil balances with the mechanical energy associated with acoustic waves. Otherwise, Galfenol saturates and exhibits no magnetostrictive responses. Thus, there exists an optimal I_0 for maximizing the magneto-mechanical coupling in the Galfenol waveguide and the signal-to-noise ratio of the Galfenol-based UT.
- **Waveguide position.** The relative position between the waveguide and the DC coil is defined by L_x, as shown in Figure 1(a). When L_x is large and the AC coil only partially covers the waveguide, the effectiveness of the DC coil degrades because the magnetic flux tends to leak at the edge of the waveguide, and the signal-to-noise ratio reduces because less Galfenol is coupled with the AC coil. When L_x is small and the AC coil sits in the middle of the waveguide, the acoustic impulse induced by the AC coil propagates along both directions and is reflected by both ends of the waveguide. This phenomenon causes interference in acoustic reflections and complicates signal processing. As a result, there exists an optimal L_x for balancing the signal-to-noise ratio and signal processing difficulties.

A set of design parameters (i.e., f_0, I_0, and L_x) was first selected manually via time-consuming trial and error. Figure 2 shows the voltage signal from the manually tuned UT in which the signal-to-noise ratio remains significant at up to the 5^{th} reflection, and the interference between the adjacent reflections is negligible. However, the design parameters are

system-dependent, and manual tuning for each and every magnetostrictive UT will prove unrealistic. Hence, a convenient, reliable model for guiding the design parameter tuning is necessary to accelerate commercialization and deployment of magnetostrictive UTs.

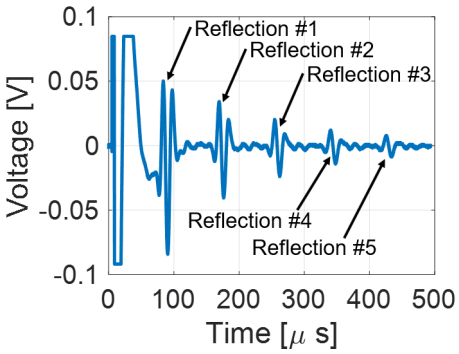

Fig. 2: Voltage measured cross the AC coil for $f_0 = 100$ kHz, $I_0 = 1$ A, and L_x = 82.5 mm.

III. Model-Guided System Tuning

An equivalent circuit model and a multiphysics finite element model were developed to facilitate the tuning of f_0, I_0, and L_x at room temperature.

A. Electrical Excitation

An equivalent circuit model (see Figure 3) first guides the selection of electrical excitation frequency f_0. For the electrical system, R_c and L_c are the resistance and inductance of the AC coil, respectively. The mechanical system is represented by a single-degree-of-freedom spring-mass damper, where k is the system stiffness, c_d is the damping coefficient, and m is the equivalent dynamic mass. This model can only target one of the system resonances or acoustic modes at a time. The magneto-mechanical coupling is described by a gyrator:

$$V_m = T\dot{y} \text{ and } f_m = Ti, \tag{1}$$

where V_m is the voltage induced across the AC coil, due to the Villari effect; T is the magneto-mechanical coupling coefficient; $\dot{y}$ is the velocity of the equivalent spring-mass-damper system; f_m is the force experienced by the waveguide, due to the Joule effect; and i is the current through the AC coil.

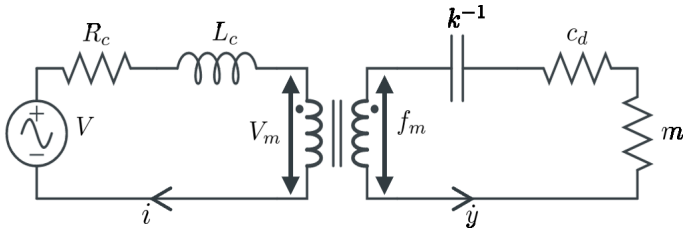

Fig. 3: Equivalent circuit model for magnetostrictive UTs.

Using the Laplace transform and Kirchhoff's law, the system function can be written in matrix format as:

$$\begin{bmatrix} V \\ 0 \end{bmatrix} = \begin{bmatrix} Z_e & T \\ -T & Z_m \end{bmatrix} \begin{bmatrix} I \\ \dot{y} \end{bmatrix}$$

where V is the excitation voltage. The electrical impedance of the magnetostrictive UT is:

$$Z_{ee} = Z_e + T^2 Z_m^{-1}, \tag{2}$$

where the contribution from the AC coil alone is $Z_e = R_c + L_c s$ and the mechanical impedance $Z_m = ms + c_d + ks^{-1}$.

The value of Z_{ee} was characterized using an impedance analyzer (Keysight E4990A). At low frequency (20 Hz), $Z_{ee} \approx R_c$. The AC coil impedance Z_{ee} was then measured between 50 and 90 kHz. As shown in Figure 4, when the excitation frequency is far away from the mechanical resonances of the waveguide (highlighted in red), the magneto-mechanical coupling is negligible, and $Z_{ee} \approx Z_e$. Therefore, the value of L_c is obtained by curve-fitting the Z_{ee} in the selected regions. The coil parameters R_c and L_c are independent from the mechanical impedance and are applicable to the entire frequency range. Three resonances are observed at around 58, 69, and 82 kHz, as shown in Figure 4. However, the spring-mass-damper model can only handle one resonance at a time. In this study, the coupling coefficient T and other mechanical parameters are identified for the resonance at 69 kHz by fitting the Z_{ee} data between 65 and 75 kHz to Eq. (2). The identified model parameters are summarized in Table I. The modeling result is compared to experimental data in Figure 5(a). A transfer function $TF(s)$ is then defined to describe the relationship between acoustic signal strength $\dot{y}$ and electrical excitation V:

$$TF(s) = \frac{T}{T^2 + Z_e Z_m}. \tag{3}$$

As shown in Figure 5(b), the $TF(s)$ magnitude peaks, and the UT achieves the optimal signal-to-noise ratio, at f_0 = 68.8 kHz. The same method can also identify other potential UT excitation frequencies.

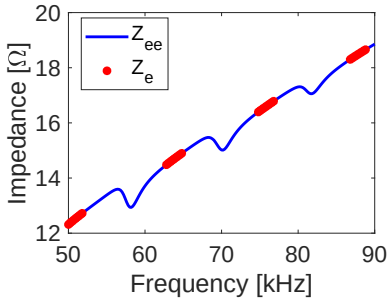

Fig. 4: Electrical impedance Z_{ee} between 50 and 90 kHz.

B. Current through the DC Coil

A 2-D-axisymmetric model was configured in COMSOL Multiphysics following the geometry presented in Figure 1(a). As with other finite element models for magnetostrictive devices in the literature [26], [27], the magnetic dynamics are

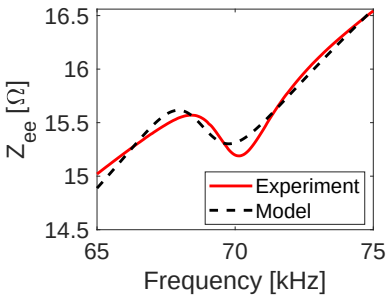

(a)

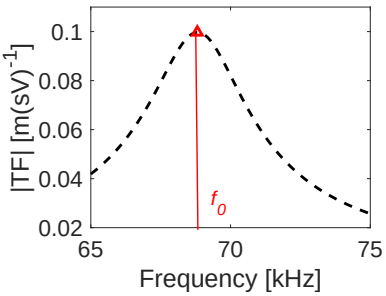

(b)

Fig. 5: (a) Model fitting results of Z_{ee}; (b) UT fundamental frequency predicted by the equivalent circuit model (f_0 = 68.8 kHz).

TABLE I: Parameters for the equivalent circuit model (for the resonance at around 69 kHz).

Parameter	Value	Parameter	Value
R_c	1.050 Ω	m	16.948 μg
L_c	35.551 μH	k	3.164 MN/m
c_d	0.365 kg/s	T	0.563

modeled for all components, as well as for the surrounding air domain, using Maxwell's equations; the mechanical dynamics are only modeled in the waveguide using Newton's second law. Because the waveguide is narrow and can hardly be magnetized along its radial direction, the magnetostrictive effect is assumed to be one-dimensional (only along the longitudinal direction); the Joule effect and the Villari effect are modeled using two separate lookup tables [26], [27]. This finite element model was first solved by a static solver to investigate the impact of the current I_0. An ideal I_0 should drive the Galfenol to its burst region, where the flux density is around 0.8 T [13], [24].

A parametric study was carried out by varying I_0 from 0 to 2.0 A in 0.1 A step sizes. To simplify the discussion, L_x is set to 82.5 mm. As shown in Figure 6, the average magnetic flux density in the coupling region (i.e., the section of Galfenol covered by the AC coil) is close to 0.8 T, and the magnetostrictive waveguide operates at its burst region when I_0 = 1.0 A. This simulation result closely matches the manual tuning outcome. Hence, the finite element model is an effective tool to predict I_0 in the future. Moreover, Figure 6 shows that severe magnetic flux leakage occurs at the end of the waveguide. By adding a soft magnetic base close to (but not in contact with) the waveguide, the magnetic flux leakage can be alleviated and the required I_0 reduced. This improvement will also enhance the magneto-mechanical transduction efficiency in the UT by offering a more uniform flux density distribution in the coupling region.

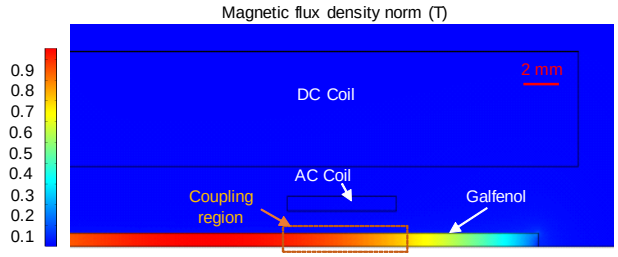

Fig. 6: Magnetic flux density distribution around the AC coil when I_0 = 1.0 A and L_x = 82.5 mm.

C. Waveguide Location

The same finite element model is then coupled with a time-dependent solver to optimize the waveguide location L_x. Other design parameters are set to I_0 = 1.0 A and f_0 = 100 kHz. A virtual spring foundation with a low stiffness of 1 Nm^{-1} is connected to the right end of the Galfenol waveguide to eliminate the rigid body motion in simulation, while capturing the free-free boundary conditions in practice. Compared to the static simulation, modeling of Galfenol-based UTs in time-domain faces additional challenges.

First, both the Joule effect and Villari effect in Galfenol depend on the magnitudes of external cyclic excitations. The magnetostrictive effect originates from the interplay between magnetic and mechanical energies. When either energy form dominates, magnetostrictive materials saturate and magnetostrictive responses no longer occur. As the cyclic stress or magnetic field are large enough to drive the magnetostrictive materials between the field- and stress-induced saturation states, magnetostrictive materials follow the so-called major loops, which are described by the lookup tables used in the current finite element model. Otherwise, the magnetostrictive materials follow minor loops, which were previously modeled via a discrete-energy-averaged constitutive model [28], [29]. Minor loops exhibit weaker magnetostrictive responses than major loops [30], [24]. Therefore, the Joule effect and Villari effect directly calculated from the lookup tables must be adjusted to avoid overpredicting the magnetostrictive UT responses. Figure 7 presents the measurement of the actual tone burst voltage pulse experienced by the AC coil when the pulse-echo transducer settings are f_0 = 100 kHz and V_0 = 100 V. Driven by this tone burst voltage, the average longitudinal stress σ_t and magnetic field H_t inside the coupling region of the Galfenol waveguide are estimated using a COMSOL model, without any major/minor loop adjustments. By feeding the resulting σ_t and H_t into the DEA model, this study discovered that the Joule effect and Villari effect minor loops induced by the tone burst voltage (see Figure 7) are 44% and 66% of their major loops, respectively. The outputs of the lookup tables in COMSOL are

adjusted accordingly to accommodate the major/minor loop discrepancy.

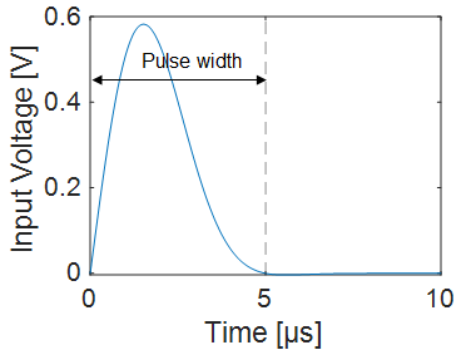

Fig. 7: A tone burst pulse wave generated by the Ultratek pulse-echo transducer when f_0 = 100 kHz and V_0 = 100 V.

The third challenge in time-domain finite element modeling is to account for the electrical dynamics in the magnetostrictive UT, including the AC coil, Ultratek pulse-echo transducer, and the electromagnetic interaction between the AC coil and the waveguide. In Figure 8, the AC coil is represented by an inductor L_c, a resistor R_c, and a voltage source V_m, following the equivalent circuit model. The pulse generation and echo-receiving features of the Ultratek system are described by a tone burst voltage source V and a resistor $R_2 = 10\ M\Omega$, respectively. The electrical circuit is initially on the pulse generation mode, or switch $SW1$ is closed and switch $SW2$ is open. Once the tone burst is complete (after 5 μs, in this case), both switches are flipped, such that the system operates in receiver mode, where R_2 denotes the receiver impedance. The voltage across R_2 is considered the system output and modeled in the time-domain at up to 500 μs, with a time step size of 0.1 μs. This simulation is repeated for a series of L_x ranging from 75 to 90 mm, in a 2.5 mm step size. The design objective is to maximize the signal-to-noise ratio while reducing the interference between adjacent reflections.

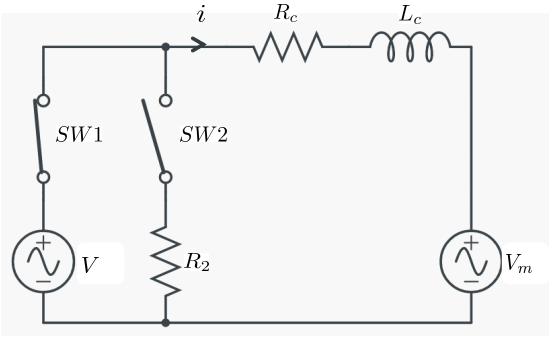

Fig. 8: Electrical circuit used in the COMSOL simulation.

Figure 9 compares the experimental and simulation results at selected L_x values. When L_x is large, the AC coil only partially covers the Galfenol waveguide, and the signal-to-noise ratio is low due to inhomogeneous magnetic flux distribution and magnetic flux leakage (see Figure 9[a]). These negative impacts are alleviated, and the signal-to-noise ratio improved, as L_x decreases and the AC coil moves toward the center of the Galfenol waveguide. Further decreasing L_x eventually has negligible impact on the signal-to-noise ratio, but reflections become indistinguishable (see Figure 9[c]). This is because the acoustic pulse generated at the coupling region propagates along both directions, and the resulting reflections interfere with each other when returning to the coupling region. Overall, the finite element simulation accurately predicted signal waveforms, despite changes in L_x. The discrepancy is more significant at small values of L_x, because any small modeling error in phase will cause large mismatches in wave interference predictions. The finite element model confirms our previous manual tuning result: a good balance between signal-to-noise ratio and reflection interference is achieved when L_x = 82.5 mm. To further reduce L_x and enhance the signal-to-noise ratio, one potential modification is to add a damping mechanism to the right end of the waveguide and eliminate the reflection interference.

D. Signal Processing

The Ultratek pulse-echo transducer delivers an electrical energy to the AC coil. Part of this energy is converted to acoustic vibrations through the electromagnetic coupling and the Joule effect. The rest of the energy is stored up on the AC coil and gradually released back to the Ultratek receiver. Experimental results show that this energy discharge procedure lasts for 100–120 μs. However, the first reflection arrives within 90 μs. Therefore, the first reflection is unreliable and must be removed from the time-of-flight calculation. Previous studies used the Hilbert transform to process the acoustic data and identify the time of flight in the time domain [17]. However, the Hilbert transform introduced relatively large measurement uncertainties. This study implements wavelet analysis and identifies acoustic wave positions in the frequency domain.

To mimic the hardware filtering in experiments, the modeled voltage data were run through a band-pass filter with half-power frequencies at 26 kHz and 4 MHz. Both the experimental and modeling results were processed using a perfect symmetric Morse wavelet with a time-bandwidth product of 3.01. The wavelet analysis results are compared in Figure 10. The acoustic wave is dispersive, since its fundamental frequency gradually decreases as time goes by. The wave dispersion is neglected due to the short time of flight. A cross-section cutting through the local maxima (the "A-A" view indicated in Figure 10) is replotted in Figure 11. Table II summarizes the time-of-flight data calculated between the peaks identified in Figure 11. The average times of flight from the model and the experiment are 85.1 and 84.9 μs, respectively, corresponding to a 0.24% simulation error.

IV. High Temperature Validation

A. Experimental Results and Discussion

To evaluate the performance of the developed Galfenol-based UT, a Remendur-based UT was created by replacing the Galfenol waveguide in Figure 1 with a Remendur waveguide that is 0.5 mm in radius and 126.2 mm in length. The design parameters

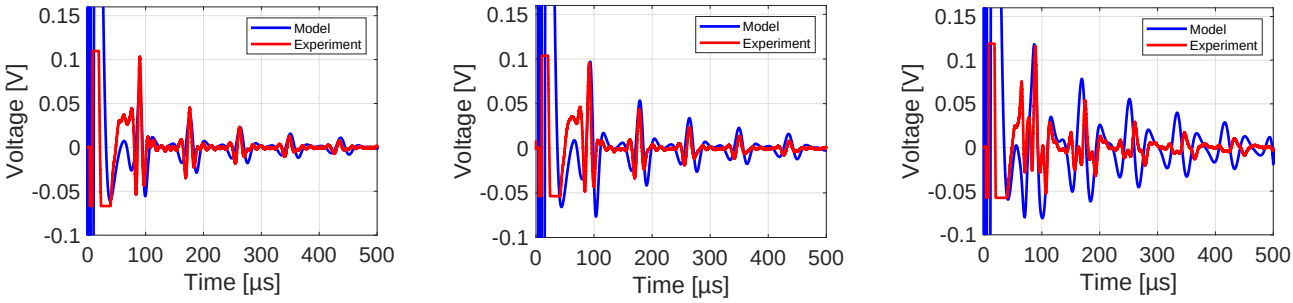

(a) (b) (c)

Fig. 9: Experimental and modeling results of magnetostrictive UT output at $I_0 = 1$ A and $f_0 = 100$ kHz, while L_x are (a) 85, (b) 82.5, and (c) 70 mm.

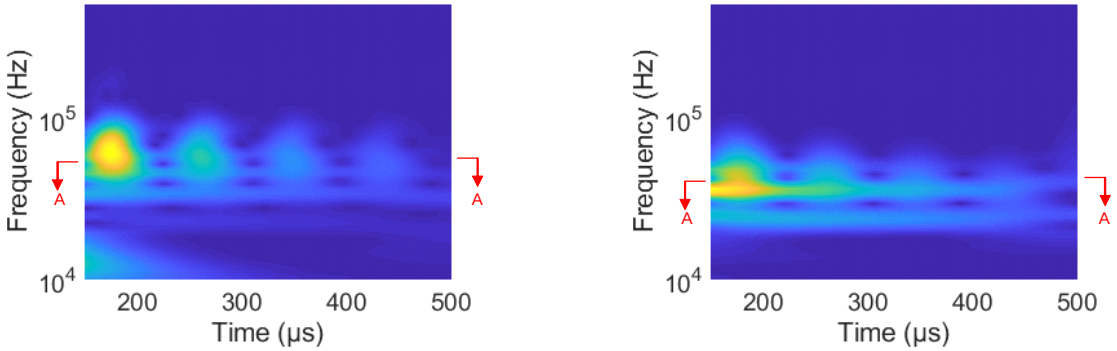

(a) (b)

Fig. 10: Wavelet analysis results for the (a) experimental data and (b) modeling results.

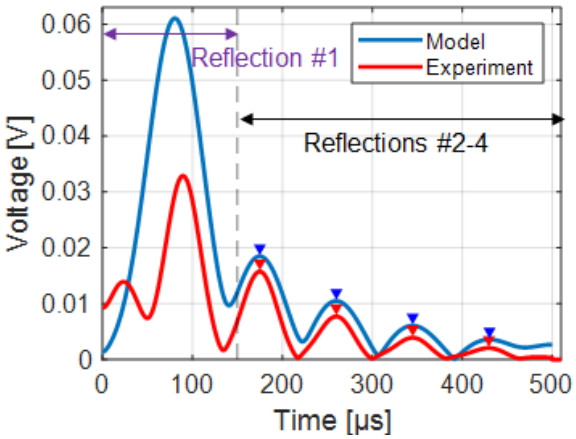

Fig. 11: Cross-section view ("A-A") of the 3-D wavelet analysis scalograms.

for the Remendur-based UT are $I_0 = 1.4$ A, $f_0 = 65$ kHz, and $L_x = 82.5$ mm, which are selected via manual tuning.

The time of arrival t_i for the ith reflection at a given temperature was obtained by following the wavelet analysis method in Section III-D. To reduce measurement uncertainty, the average time of flight Δt was then calculated as:

$$\Delta t = \frac{\sum_{i=2}^{n-1} (t_{i+1} - t_i)}{n-2}, \tag{4}$$

where n indicates the last reflection included in the data acquisition and $n = 5$ in this study. Figure 12 shows Δt as measured from the Galfenol- and Remendur-based UTs at different temperatures. Through linear regression, the temperature-varying Δt is fitted by a straight line whose slope is k_t. The

TABLE II: Time-of-flight results at room temperature, obtained via experiments and simulation using the wavelet analysis.

Experiment		
Reflection #	Time (μs)	Time of flight (μs)
2	174.8	
3	259.8	85.0
4	344.7	84.9
5	429.4	84.7
	Average (μs)	84.9
Simulation		
Reflection #	Time (μs)	Time of flight (μs)
2	174.9	
3	260.0	85.1
4	344.9	84.9
5	430.3	85.4
	Average (μs)	85.1

UT sensitivity is then calculated as:

$$S = k_t/\Delta t_0, \tag{5}$$

where Δt_0 is the time of flight at room temperature T_0. The linearity of magnetostrictive UTs is described by the coefficient of determination R^2. The temperature measurement resolution δT is derived from:

$$\delta T = \frac{1}{f_s \Delta t_0 S}, \tag{6}$$

where f_s is the sampling frequency. The measurement resolution improves with respect to increasing f_s. Due to the limited buffer size, an excessive f_s results in a short measurement duration, leads to a small n value, and introduces more uncertainties in Δt measurement. Therefore, the sampling frequency was set to 80 MHz in this study.

The relative measurement uncertainty at a given temperature is quantified by:

$$\eta = \frac{\sqrt{\delta t}}{\Delta t_0 S T_0}, \tag{7}$$

where δt is the variance in Δt measurement.

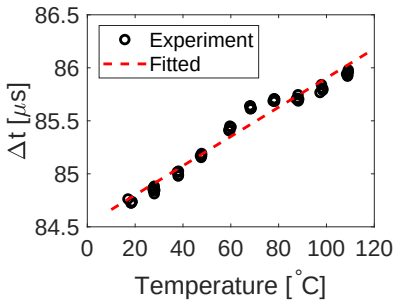

(a)

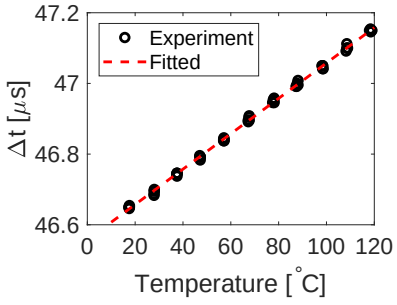

(b)

Fig. 12: Time of flight versus ambient temperature from the (a) Galfenol-based UT and (b) Remendur-based UTs.

TABLE III: Performance of Galfenol- and Remendur-based UTs.

	Sensitivity ($\times 10^{-6}$/°C)	R^2 (-)	Resolution (°C)	Uncertainty (%)
Galfenol UT	162.8	96.1	0.45	2.9
Remendur UT	107.3	99.9	1.25	1.9

Table III compares UT performance in terms of sensitivity, linearity, resolution, and measurement uncertainty. The Galfenol-based UT exhibits a sensitivity 51.7% higher than that of the Remendur-based UT. Under the same sampling frequency, the measurement resolution of the Galfenol-based UT is 64% smaller. The Remendur-based UT exhibits superior linearity, while the Galfenol-based UT exhibits significant nonlinearity at 70–90°C. Theoretically:

$$\Delta t = 2L_w\sqrt{\frac{\rho_w}{E_w}}, \tag{8}$$

where L_w, ρ_w, and E_w are the length, density, and Young's modulus of the waveguide, respectively. As temperature increases, L_w increases and ρ_w reduces due to thermal expansion, while E_w decreases due to the reducing inter-atomic forces. Both the thermal expansion coefficient and Poisson's ratio of Galfenol are nonlinear functions of temperature [31]. Thus, the temperature dependencies in these parameters are complicated and have not yet been studied comprehensively.

The first potential cause of the nonlinearity in the Galfenol-based UT is that the variation in ρ_w dominates at 70–90°C. To validate this hypothesis, both longitudinal and lateral thermal expansion must be characterized within the future temperature range of interest. The second hypothesis is that the temperature-driven anelastic relaxation or phase transformation in Galfenol causes dramatic changes in E_w and induces nonlinearity in Δt measurement [32]. The anelasticity and phase transformation also cause nonlinearity in material damping. Therefore, the waveguide damping, as described in terms of the acoustic attenuation coefficient α, is analyzed to preliminarily validate this hypothesis. As shown in Figure 13, the envelopes are found through the Hilbert transform, and the acoustic signal strength is depicted by A_i, which is the envelope peak associated with the i^{th} reflection.

$$\alpha = \frac{-1}{6L_w}\sum_{i=2}^{4} 20\log_{10}\left(\frac{A_{i+1}}{A_i}\right), \tag{9}$$

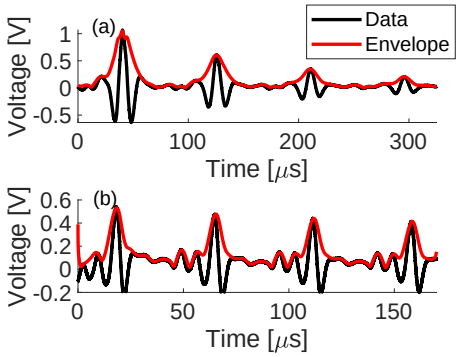

Fig. 13: Envelopes enclosing signals between the 2^{nd} and 5^{th} reflections: (a) Galfenol- and (b) Remendur-based UTs.

Figure 14 shows the acoustic attenuation coefficient as a function of temperature for both the Galfenol and Remendur waveguides. Overall, the Galfenol waveguide exhibits much more significant damping, since it has a larger diameter and experiences more severe eddy currents. It is also noted that Remendur shows temperature invariant

damping, while α in Galfenol peaks at around 80°C. This nonlinear damping matches the temperature-driven anelastic effect previously observed in Galfenol, thus preliminarily supporting the second hypothesis. However, a more comprehensive high-temperature material characterization (e.g., differential scanning calorimetry testing) is needed to confirm this conclusion.

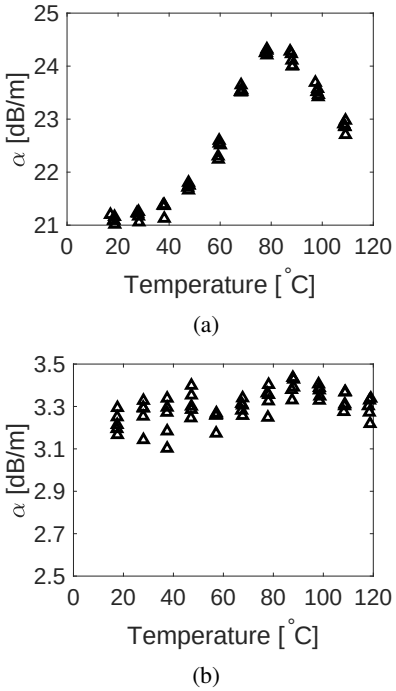

Fig. 14: Acoustic attenuation coefficient versus temperature for (a) Galfenol and (b) Remendur waveguides.

V. Conclusions

This paper prototyped a new magnetostrictive UT consisting of a Galfenol waveguide, a DC coil, and an AC coil. This ultrasonic sensor can also support the surveillance, diagnosis, and prognosis of other critical nuclear energy system parameters such as pressure, geometry changes, and structural health. Experimental validation was presented, along with an equivalent circuit model and a multiphysics finite element model. Both models accurately captured the multiphysics coupling between the mechanical, magnetic, and electrical domains. Using these models, the electrical excitation frequency, waveguide position, and biasing magnetic field were optimized to improve the signal-to-noise ratio and facilitate signal processing. The performance of the Galfenol-based UT was characterized from room temperature to 120°C. Compared to a similar Remendur-based UT, the Galfenol-based UT exhibits a higher sensitivity of $162.8\times10^{-6}/°$C, as well as superior measurement resolution at down to 0.45°C. However, the Galfenol waveguide showed more severe measurement uncertainty and more significant acoustic attenuation. Future UTs should use thinner wires (e.g., reduce the wire diameter through centerless grinding) to mitigate the eddy current loss. The Galfenol sample used in this study contained 18.4 wt.% gallium and exhibited limited ductility. The other option is to use Galfenol samples with 10 wt.% gallium that can be directly drawn into thin wires. The Galfenol-based UT also showed significant nonlinearity at around 80°C, due to nonlinear thermal expansion and/or temperature-driven anelastic effects. A more comprehensive characterization within the selected temperature range is required to sort out the origins of the nonlinearity.

References

[1] World Nuclear Association. (2021) Safety of nuclear power reactors - appendix 1. [Online]. Available: https://world-nuclear.org/information-library/safety-and-security/safety-of-plants/appendices/safety-of-nuclear-power-reactors-appendix.aspx

[2] International Atomic Energy Agency. (2019) IAEA annual report 2019. [Online]. Available: https://www.iaea.org/sites/default/files/publications/reports/2019/gc64-3.pdf

[3] B. G. Kim, J. L. Rempe, J.-F. Villard, and S. Solstad, "Review of instrumentation for irradiation testing of nuclear fuels and materials," *Nuclear Technology*, vol. 176, no. 2, pp. 155–187, 2011.

[4] A. L. Legrand and J. F. Villard, "Noise thermometry for nuclear applications," *ANIMMA 2009 - 2009 1st International Conference on Advancements in Nuclear Instrumentation, Measurement Methods and their Applications*, 2009.

[5] M. Laurie, D. Magallon, J. Rempe, C. Wilkins, J. Pierre, C. Marquié, S. Eymery, and R. Morice, "Ultrasonic high-temperature sensors: past experiments and prospects for future use," *International Journal of Thermophysics*, vol. 31, no. 8-9, pp. 1417–1427, 2010.

[6] R. Van Nieuwenhove and S. Solstad, "In-core fuel performance and material characterization in the halden reactor," in *2009 1st International Conference on Advancements in Nuclear Instrumentation, Measurement Methods and their Applications*. IEEE, 2009, pp. 1–7.

[7] D. Knudson, J. Rempe, and J. Daw, "Evaluation of candidate linear variable displacement transducers for high temperature irradiations in the advanced test reactor," Idaho National Laboratory (INL), Tech. Rep., 2009.

[8] B. Reinhardt, J. Daw, and B. Tittmann, "Irradiation testing of piezoelectric (aluminum nitride, zinc oxide, and bismuth titanate) and magnetostrictive sensors (remendur and galfenol)," *IEEE Transactions on Nuclear Science*, vol. 65, no. 1, pp. 533–538, 2017.

[9] L. Lynnworth, E. Carnevale, M. McDonough, and S. Fam, "Ultrasonic thermometry for nuclear reactors," *IEEE Transactions on Nuclear Science*, vol. 16, no. 1, pp. 184–187, 1969.

[10] G. Carlson and H. G. Plein, "Refractory metals for ultrasonic thermometry application," Sandia Labs., Tech. Rep., 1978.

[11] P. G. Evans, "Nonlinear magnetomechanical modeling and characterization of Galfenol and system-level modeling of Galfenol-based transducers," Ph.D. dissertation, The Ohio State University, 2009.

[12] R. A. Kellogg, A. Flatau, A. E. Clark, M. Wun-Fogle, and T. Lograsso, "Quasi-static transduction characterization of Galfenol," in *ASME International Mechanical Engineering Congress and Exposition*, vol. 37076, 2003, pp. 273–280.

[13] Z. Deng, "Nonlinear modeling and characterization of the Villari effect and model-guided development of magnetostrictive energy harvesters and dampers," Ph.D. dissertation, The Ohio State University, 2015.

[14] M. J. Dapino, R. C. Smith, F. T. Calkins, and A. B. Flatau, "A coupled magnetomechanical model for magnetostrictive transducers and its application to Villari-effect sensors," *Journal of intelligent material systems and structures*, vol. 13, no. 11, pp. 737–747, 2002.

[15] J. Daw, B. Tittmann, and B. Reinhardt, "Ultrasonic transducers for harsh environments," Idaho National Lab.(INL), Idaho Falls, ID (United States), Tech. Rep., 2016.

[16] J. Daw, J. Palmer, P. Ramuhalli, P. Keller, R. Montgomery, H.-T. Chien, G. Kohse, B. Tittmann, B. Reinhardt, and J. Rempe, "Ultrasonic transducer irradiation test results," Idaho National Lab.(INL), Idaho Falls, ID (United States), Tech. Rep., 2015.

[17] J. Daw, J. Rempe, J. Palmer, P. Ramuhalli, R. Montgomery, H. T. Chien, B. Tittmann, B. Reinhardt, and P. Keller, "NEET in-pile ultrasonic sensor enablement-final report," Idaho National Laboratory (INL), Tech. Rep., Sep. 2014. [Online]. Available: https://www.osti.gov/biblio/1166037

[18] A. E. Nolting and E. Summers, "Tensile properties of binary and alloyed Galfenol," *Journal of Materials Science 2015 50:15*, vol. 50, pp. 5136–5144, 5 2015. [Online]. Available: https://link.springer.com/article/10.1007/s10853-015-9045-6
[19] O. Kubaschewski, *Iron—Binary phase diagrams*. Springer Science & Business Media, 2013.
[20] N. Kawamiya, K. Adachi, and Y. Nakamura, "Magnetic properties and mössabauer investigations of Fe-Ga alloys," *Journal of the Physical Society of Japan*, vol. 33, no. 5, pp. 1318–1327, 1972.
[21] A. E. Clark, M. Wun-Fogle, J. B. Restorff, and T. A. Lograsso, "Magnetostrictive properties of Galfenol alloys under compressive stress," *Materials transactions*, vol. 43, no. 5, pp. 881–886, 2002.
[22] R. A. Kellogg, "Development and modeling of iron-gallium alloys," Ph.D. dissertation, Iowa State University, 2003.
[23] Z. Deng and M. J. Dapino, "Magnetic flux biasing of magnetostrictive sensors," *Smart Materials and Structures*, vol. 26, p. 055027, 4 2017. [Online]. Available: https://iopscience.iop.org/article/10.1088/1361-665X/aa688b https://iopscience.iop.org/article/10.1088/1361-665X/aa688b/meta
[24] Z. Deng, J. J. Scheidler, V. M. Asnani, and M. J. Dapino, "Quasi-static major and minor strain-stress loops in textured polycrystalline $Fe_{81.6}Ga_{18.4}$ Galfenol," *Journal of Applied Physics*, vol. 120, no. 24, p. 243901, 2016.
[25] R. A. Kellogg, A. Flatau, A. E. Clark, M. Wun-Fogle, and T. Lograsso, "Quasi-static transduction characterization of Galfenol," *American Society of Mechanical Engineers, Aerospace Division (Publication) AD*, vol. 68, pp. 273–280, 5 2008.
[26] Z. Deng and M. J. Dapino, "Influence of electrical impedance and mechanical bistability on Galfenol-based unimorph harvesters," *Journal of Intelligent Material Systems and Structures*, vol. 28, no. 3, pp. 421–431, 2017.
[27] Z. Deng and M. J. Dapino, "Modeling and design of Galfenol unimorph energy harvesters," *Smart Materials and Structures*, vol. 24, no. 12, p. 125019, 2015.
[28] P. G. Evans and M. J. Dapino, "Efficient magnetic hysteresis model for field and stress application in magnetostrictive Galfenol," *Journal of applied physics*, vol. 107, no. 6, p. 063906, 2010.
[29] Z. Deng and M. J. Dapino, "Characterization and finite element modeling of Galfenol minor flux density loops:," *http://dx.doi.org/10.1177/1045389X14521703*, vol. 26, pp. 47–55, 2 2014.
[30] L. Weng, T. Walker, Z. Deng, M. Dapino, and B. Wang, "Major and minor stress-magnetization loops in textured polycrystalline $Fe_{81.6}Ga_{18.4}$ Galfenol," *Journal of Applied Physics*, vol. 113, no. 2, p. 024508, 2013.
[31] J.-H. Yoo and A. B. Flatau, "Measured iron-gallium alloy tensile properties under magnetic fields," in *Smart Structures and Materials 2004: Active Materials: Behavior and Mechanics*, vol. 5387. International Society for Optics and Photonics, 2004, pp. 476–486.
[32] S. Jen, Y. Lo, and L. Pai, "Temperature dependence of mechanical properties of the $Fe_{81}Ga_{19}$ (Galfenol) alloy," *Journal of Physics D: Applied Physics*, vol. 49, no. 14, p. 145004, 2016.

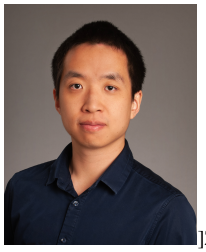

[ ]Zhangxian Deng is an assistant professor in the Department of Mechanical and Biomedical Engineering at Boise State University. He joined to the department in July 2018. Before coming to Boise State University. Dr. Deng was a postdoctoral researcher at the NSF IUCRC Smart Vehicle Concepts Center. The fundamental goal of Dr. Deng's research is to tackle challenging engineering problems by utilizing novel functional/smart materials, including magnetostrictive, piezoelectric, shape memory, and magneto-rheological materials.

[ ]Amanda White is a graduate research assistant in the Department of Mechanical and Biomedical Engineering at Boise State University. She is currently pursuing a Masters of Mechanical and Biomedical Engineering degree. She received her Bachelors of Science in Mechanical Engineering at Boise State University. Prior to performing research on smart materials under Dr. Deng, Ms. White published research on cold atmospheric pressure plasma devices.